PAPER

Check for updates

Synthesis, characterization, and evaluation of PEGylated first-row transition metal ferrite nanoparticles as T_2 contrast agents for high-field MRI†

Abhinandan Banerjee, [ID] [a] Barbara Blasiak, [bc] Eva Pasquier, [ad] Boguslaw Tomanek [bce] and Simon Trudel [ID] *[a]

Poly(ethylene glycol) (PEG)-coated transition metal ferrite (MFe$_2$O$_4$; M = Co, Cu, Fe, Mn, Ni, Zn) nanoparticles (NPs) were generated by a one-pot synthetic protocol and found to be small, fairly monodisperse, and superparamagnetic in nature. When evaluated for high-field magnetic resonance imaging, these showed high values of r_2 and r_2/r_1 at 9.4 T. The well-documented biocompatibility of PEG coatings makes these NPs attractive candidates as T_2 contrast agents for high-field MRI. A systematic comparison of magnetic and relaxivity measurements reveals MnFe$_2$O$_4$ and CoFe$_2$O$_4$ NPs to be superior T_2 MRI contrast agents compared to Fe$_3$O$_4$ NPs.

1 Introduction

Magnetic resonance imaging (MRI) is one of the best established imaging modalities in preclinical research and clinical diagnosis, owing to the use of non-ionizing radiation, high resolution, superior soft-tissue contrast, and the non-invasive nature of the technique.[1–3] Most MRI investigations in clinical settings use contrast agents – magnetic species administered to the patient prior to imaging – for contrast improvement.[4] While gadolinium chelates are traditionally used to shorten the longitudinal relaxation time of water protons in tissues – thereby generating a brighter image (hyperintense MRI) – the nephrotoxicity of gadolinium-based contrast media, especially in patients with chronic renal failure,[5] makes it essential to explore alternative contrast agents.

Recent advances in nanoscience have made magnetic nanoparticles (NPs) with customized attributes such as size, shape, composition, and surface functionalizations attractive

candidates for MRI contrast agents.[6–8] NP contrast agents offer an additional advantage over gadolinium chelates; they can increase the transverse relaxation rates of water protons in the system being imaged, leading to darker images in T_2-weighted MRI,[9] in addition to the protocol mentioned previously.[10] Furthermore, these NPs allow enhanced tumor detection using susceptibility-weighted imaging.[11] There are examples of nanocomposites functioning as bifunctional $T_1 - T_2$ contrast agents.[12] Surface-capped iron oxide nanoparticles have been shown to be very effective for MRI contrast enhancement.

From the theory of MRI, it is evident that the available signal, which is ultimately converted to an image, strongly depends on the static magnetic field strength ($B_0 = \mu_0 H$).[1] Most clinical MRI scanners operate at field strengths between 1.5 and 3 T. However, recent developments in magnet fabrication and shielding allowed 7–9.4 T scanners to be applied for whole-body imaging.[13,14] The advantages of high-field MRI are manifold: higher signal-to-noise ratio, as well as improved spectral resolution for certain applications.[15,16] Evidently, these improvements facilitate higher spatial and/or temporal resolution than previously possible with MRI. While the technological, physical and safety limitations of high-field and ultra-high-field MRI are still being investigated, the time is ripe for increased research into high-field contrast agents as their efficacy strongly depends on the magnetic field strength[17] which could be used under these conditions to further improve image quality and contrast. Obviously, NP-based contrast agents are expected to play a major role in high-field MRI.[18,19]

Given the number of potential factors that can affect the type of contrast (*e.g.*, T_1, T_2, T_2^*, or $T_1 - T_2$) and field-suitability (low, intermediate, high, ultra-high, or overlapping combinations

[a]Department of Chemistry, Institute for Quantum Science and Technology, University of Calgary, 2500 University Dr NW, Calgary, AB, T2N 1N4, Canada. E-mail: trudels@ucalgary.ca

[b]Department of Clinical Neurosciences, University of Calgary, 3330 Hospital Dr NW, Calgary, AB T2N 4N1, Canada

[c]Institute of Nuclear Physics, Polish Academy of Sciences, 152 Radzikowskiego, Krakow, 31-342, Poland

[d]École Européenne de Chimie, Polymères et Matériaux de Strasbourg (ECPM), 25 Rue Becquerel, 67087 Strasbourg, France

[e]Oncology Department, University of Alberta, 8303-112 St., Edmonton, AB T6G 2T4, Canada

thereof) of nanoparticulate contrast agents, it is unsurprising that a vast number of studies have focused on modifying one or more of the relevant NP properties in order to synthesize MRI contrast agents for specific applications. Jun *et al.*, for instance, synthesized iron oxide NPs of varying sizes to support their hypothesis that larger NPs show greater saturation magnetisation (M_s), and consequently, higher T_2 relaxivity.[20] Similarly, iron oxide NP clusters encapsulated in poly(ethylene oxide-*co*-lactide) or silica have shown transverse relaxivity (r_2) values that are approximately double that of the commercially available iron oxide NP-based MRI contrast agent Ferridex®.[21] Functional-group-appended PEG was used by Gao and colleagues to cap iron oxide NPs in a post-synthetic surface modification step; these showed moderate r_2 values in the range of 24 to 48 mM^{-1} s^{-1} for 3.6 nm iron oxide NPs, and 80–92 mM^{-1} s^{-1} for 10.9 nm iron oxide NPs.[22] Shape, too, has been taken into consideration as a potential customization factor for enhancing the contrasting abilities of iron oxide NPs. In one of the most widely cited examples, octapod Fe_3O_4 NPs with sub-50 nm edges showed an outstanding r_2 value of 679 mM^{-1} s^{-1}.[23] In a study by Hegmann and colleagues, Triton-X coated brick-shaped Fe_3O_4 NPs also showed very high r_2 values and r_2/r_1 ratios.[24] One-dimensional nanostructures of iron oxide have also been known to exhibit tunable r_1 and r_2 values: ultra-thin iron oxide nanowhiskers coated with the surfactant Tween-80 were found to have $r_1 = 6.13$ mM^{-1} s^{-1} and $r_2 = 11.15$ mM^{-1} s^{-1},[25] while 70 nm long Fe_3O_4 nanorods capped with poly-ethyleneimine showed very high r_2 values of 608 mM^{-1} s^{-1}.[26]

Given that the proton spin–spin relaxation rate R_2 in the presence of NP contrast agents depends, among other things, on the thickness of the capping agent coating the NP surface, attempts have been made to improve the contact between the magnetic core and the water molecules in organs being imaged by selecting a small, hydrophilic NP-capping molecule.[17] Small molecules that are expected to be bio-compatible, such as ascorbate, citrate, other carboxylic acids,[27] glutathione,[28] and dopamine,[29] are being extensively studied to this end. Recently, we showed that maltol, an FDA-approved pharmaceutical additive that enhances the bioavailability of iron *in vivo*, is a suitable capping agent for obtaining efficient T_2 contrast agents at both clinical and high fields with demonstrated inertness to human cell lines.[30] It is to be noted that direct incorporation of a molecular (as opposed to a polymeric) capping agent on the NP surface during the formative stage may call for milder synthetic conditions to maintain the integrity of the capping agent, which may lead to reduced phase purity and magnetic behaviour of the ferrite nanocrystals formed. To avoid this, a two-stage synthesis is often used, initially generating a hydrophobic NP surface under harsher reaction conditions, which is then subjected to a post-synthetic ligand exchange regime, in order to render the NPs water soluble.[31,32]

In this comparative study, poly(ethylene glycol) (PEG) was selected as a simple, well-studied, and biocompatible NP-stabilizing ligand,[33,34] in order to divert attention from the ligand shell, and focus on the metal oxide core. While several individual reports on specific compositions of metal–ferrite NPs can be found in the relevant literature, there are only a few

systematic studies where the composition is the primary variable under investigation. In a pioneering study by Cheon and co-workers, MFe_2O_4 NPs (M = Ni, Co, Fe, and Mn) were synthesized by a high-temperature reaction between the divalent metal chloride and iron(III) 2,4-pentadionate in the presence of oleic acid and oleylamine, followed by a surface ligand exchange and antibody conjugation.[35] It was noted that the M_s and contrasting abilities of these NPs (at $B_0 = 1.5$ T) increased as a function of the divalent metal in the following order: Mn > Fe > Co > Ni. Another significant study which explicitly investigates the high-field relaxivities of succimer-coated MFe_2O_4 NPs (M = Co, Mn, Fe) was performed by Brazel and colleagues in 2009; this study found $CoFe_2O_4$ NPs to be the best T_2 contrast agent of the three, with $r_2/r_1 = 62.3$.[36] In 2015, Bokias and colleagues encapsulated oleylamine-capped $MnFe_2O_4$, $CoFe_2O_4$, and $NiFe_2O_4$ NPs into the hydrophobic cores of spherical micellar structures formed by linear and comb-like co-polymers in an aqueous solution to generate colloidal superparticle structures; the r_2 relaxivity of these systems under 1.5 T and 3 T magnetic fields followed the order Co > Mn > Ni. Comb-type co-polymer enshrouded $CoFe_2O_4$ NPs showed the highest r_2 values (316.0 mM^{-1} s^{-1}).[37]

The present communication aims to augment these existing examples by providing a systematic study of the late 3d transition metal ferrite NPs *via* magnetometric and high-field relaxometric measurements. The spin–spin relaxation rate R_2 is given as[38,39]

$$R_2 = \frac{1}{T_2} = \frac{256\pi^2\gamma^2}{405} \frac{\kappa m_s^2 a^2}{D\left(1 + \frac{L}{a}\right)} \tag{1}$$

where a is the magnetic radius core, L is the impermeable coating thickness, γ is the gyromagnetic ratio of the proton, m_s is the saturation magnetization of the NP sample, $\kappa = V^*/C$ where V^* is the volume fraction of the magnetic core and C is the concentration of magnetic atoms, and D is the diffusion coefficient of water molecules. Looking in the literature, one often finds two or more variables being changed from study to study (*e.g.*, morphology and state of aggregation, or nature of surface coating and size), making direct comparisons and benchmarking difficult. However, if the parameters are kept fairly constant (NP size, same ligand), then the effect of changing the divalent ion on the MRI properties of different MFe_2O_4 NPs can be studied in a consistent manner. In particular, looking at eqn (1), it then appears the saturation magnetization should be the determining factor – which is known to depend on the divalent ion in spinel ferrites[40] – with higher magnetization expected to yield to higher r_2 values. We indeed find that at high fields ($B_0 = 9.4$ T) the transverse relaxivity r_2 increases from Cu < Ni < Zn < Fe < Co < Mn while the ratio of the transverse to longitudinal relaxivities r_2/r_1 follows the Cu < Ni < Zn < Fe < Mn < Co trend.

2 Experimental section

2.1 Materials

The metal precursors – manganese(II), iron(III), cobalt(II), nickel(II), and zinc(II) 2,4-pentadionate, and copper(II) chloride

dihydrate – were purchased from Strem Chemicals, and used as received. Poly(ethylene glycol) ($M_n = 400$, PEG$_{400}$) and NaBH$_4$ (≥98%) were obtained from Sigma Aldrich. All reactions were carried out in clean oven-dried glassware, under an atmosphere of nitrogen.

2.2 Synthesis

PEGylated MFe$_2$O$_4$ NPs were generated using a highly modified reductive synthetic protocol.[41] In a representative synthesis, Co(acac)$_2$ (171 mg, 0.67 mmol) and Fe(acac)$_3$ (472 mg, 1.33 mmol) were dissolved in 25 mL of PEG$_{400}$. Nitrogen was bubbled through the solution for 30 min. The solution was then taken in a three-necked flask fitted with a reflux condenser, heated with a J-KEM Scientific Gemini PID temperature controller to 170 °C and maintained at this temperature for 15 minutes. A separate solution of NaBH$_4$ (162 mg, 5 mmol) dispersed in *ca.* 5 mL of PEG$_{400}$ was vigorously stirred under nitrogen. The reaction flask was cooled from 170 to 100 °C, and the NaBH$_4$ dispersion was added all at once to the metal acetylacetonate solution at 100 °C, leading to brisk effervescence, and immediate darkening of color from orange to brown-black. This mixture was stirred at 170 °C for an additional 30 min, and then allowed to cool to 100 °C. A slight stoichiometric excess of water (approx. 5 mL) was added to the solution to quench unreacted NaBH$_4$. The system was then heated to 150 °C and maintained at that temperature for an additional 5 h, after which heating was removed, and the flask cooled to room temperature. The system was opened to air, and the black product was precipitated overnight from the reaction mixture with a large excess of ethyl acetate (approx. 200 mL). The mixture was centrifuged (6000 rpm, 10 min) and the supernatant decanted and discarded. This washing process was repeated thrice, *via* the addition of fresh portions (approx. 40 mL) of ethyl acetate, centrifugation, and removal of supernatant. Finally, the nanoparticles were air-dried at room temperature, and stored in tightly capped glass vials under air. The amounts of divalent metal precursor used in the other syntheses are presented in Table S1.†

2.3 Transmission electron microscopy (TEM)

TEM imaging was performed with a Hitachi H7650 microscope operated at 100 kV. Powdered samples were dispersed in methanol and drop-cast onto a carbon-coated copper grid (Ted Pella) and left to dry in air. Images were analyzed using ImageJ.[42]

2.4 Powder X-ray diffraction (PXRD)

A Bruker D8 ECO Advance powder diffractometer (Cu K$_\alpha$ = 1.5406 Å, 40 kV, 40 mA) was used for phase identification. The sample was suspended in ether and smeared on a zero-background silicon sample plate (Si, P-type, B-doped; MTI Corp.). Intensity was measured in the $2\theta = 25$–$75°$ range.

2.5 Fourier-transform infrared spectroscopy

Infrared spectra of nanoparticles in a KBr disk were collected on a Nicolet Nexus 470 spectrometer.

2.6 Energy dispersive X-ray spectroscopy (EDXS)

A Zeiss ΣigmaVP field-emission scanning electron microscope operated at 20 kV equipped with an Oxford INCA EDXS unit was used to determine the composition of the nanoparticles. Samples were prepared by dropping *ca.* 5 mg of powder onto double-sided adhesive conductive carbon tape, which was fixed on standard aluminum stubs.

2.7 Zeta potential measurement

Zeta potentials of PEGylated MFe$_2$O$_4$ NPs in aqueous solutions were measured at pH 7 using disposable folded capillary zeta cells in a Malvern Zetasizer Nano ZS dynamic light scattering system. For time-dependent measurements, the cuvette remained undisturbed in the instrument for the requisite length of time.

2.8 Superconducting quantum interference device (SQUID) magnetometry

Magnetic properties of the samples were measured using a Quantum Design XL-7S MPMS. Samples were prepared by placing a weighed quantity of powdered sample into a gelatin capsule, which was inserted in a clear, diamagnetic plastic straw. $M(\mu_0 H)$ measurements were conducted at temperatures of 1.9 K and 300 K in a maximal field strength of 4 T. For measurements at the physiological temperature, taken to be 310 K, the maximum field strength was extended to 7 T to mimic the conditions of high-field MRI. Zero-field-cooled (ZFC) magneti-zation of the sample was measured between temperatures of 1.9 and 300 K in a field of 10 mT, after the sample had been cooled in the absence of a magnetic field. Field-cooled (FC) measure-ments were done as for the ZFC measurement, however the sample was cooled from 300 K in the presence of a 10 mT magnetic field.

2.9 9.4 T MRI experiments

T_1 and T_2 relaxation measurements and phantom images were obtained using a 9.4 T/21 cm magnet (Magnex, UK) and a Bruker console (Bruker, Germany). Standard 5 mm diameter NMR tubes were used for experiments. A transmit/receive radio frequency (RF) volume birdcage coil was applied. A single slice multi-echo pulse sequence was used for T_2 measurements with the following parameters: repetition time (T_R) = 7.5 s, 1 average, matrix size 128 × 128, field of view (FOV) 3 cm × 3 cm, slice thickness 2 mm, 64 echoes 4 ms apart. The T_2 relaxation time was calculated using a single exponential fitting of the echo train (Bruker, Germany). For T_1 measurements the TRUE FISP method was used with the following parameters: slice thickness 2 mm, FOV 3 × 3 cm, 1 average, matrix size 128 × 128, echo time (T_E) = 1.5 ms, T_R = 1 s.

The relaxivity values (r_1, r_2) were determined from relaxation times measured at different concentrations from the following equation:

$$T_i^{-1} = T_{0,i}^{-1} + r_i C \tag{2}$$

where T_i are the observed relaxation times in the presence of magnetic nanoparticles, $T_{0,i}$ is the relaxation time of pure water, and C is the concentration of magnetic ions in the PEGylated MFe_2O_4 NPs. The subscripts indicate longitudinal ($i = 1$) or transverse ($i = 2$) relaxivities and relaxation times, respectively.

3   Results and discussion

3.1   Synthesis

We report a novel synthesis of mixed-metal ferrites in neat PEG (Fig. 1). As may be expected from their PEG coatings, the NPs were highly soluble in water. This synthesis has the advantage of simplicity, using simple reactants and a single-pot protocol. The chemistry is general, and worked with all metal precursors used, yielding phase-pure samples (*vide infra*). The exception was $CuFe_2O_4$, which is also seen to contain elemental Cu in addition to $CuFe_2O_4$ (identified in Fig. 2 with asterisks). $CuFe_2O_4$ NPs synthesized from $Cu(acac)_2$ showed prominent impurity peaks showing the presence of copper and iron oxides (not shown), which is documented.[43] The presence of secondary phases was minimized (but not eliminated) by using $CuCl_2$-·$2H_2O$ as a copper source, as recommended by Ros and colleagues.[44] The size distributions are not quite monodisperse, with ratios of the standard deviation over the mean of approx. 20% (by this metric, a value smaller than 10% would be required for a sample to be deemed monodisperse). It is anticipated that size can be controlled in these systems by varying the ratio of reducing agent to metal precursor.

This synthesis was inspired by a reductive synthesis of Fe_3O_4 NPs.[30,41] In the initial report,[41] Yathindranath *et al.* describe a reductive step to form the divalent Fe^{2+} cations necessary for the formation of the spinel structure. In our case, no such reductive step is required as the divalent cation is directly supplied. Nonetheless, the addition of $NaBH_4$ triggers the nucleation of MFe_2O_4 NPs. We surmise $NaBH_4$ reacts with adventitious water or end groups of the PEG polymer chains to form hydroxyl ions, which form intermediate metal hydroxides ($Fe(OH)_3$ and $M(OH)_2$) that condense and dehydrate to form the oxide, regenerating water. No NPs were obtained in a control experiment setting which omitted the addition of $NaBH_4$ to the reaction mixture.

3.2   Structural characterization

PXRD measurements were performed to determine the phase of MFe_2O_4 NPs. Fig. 2 shows typical XRD patterns of the various
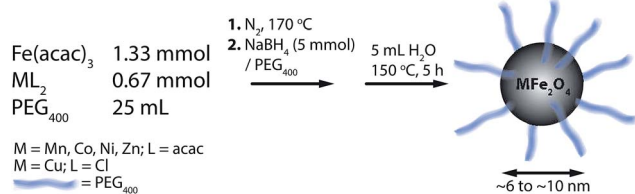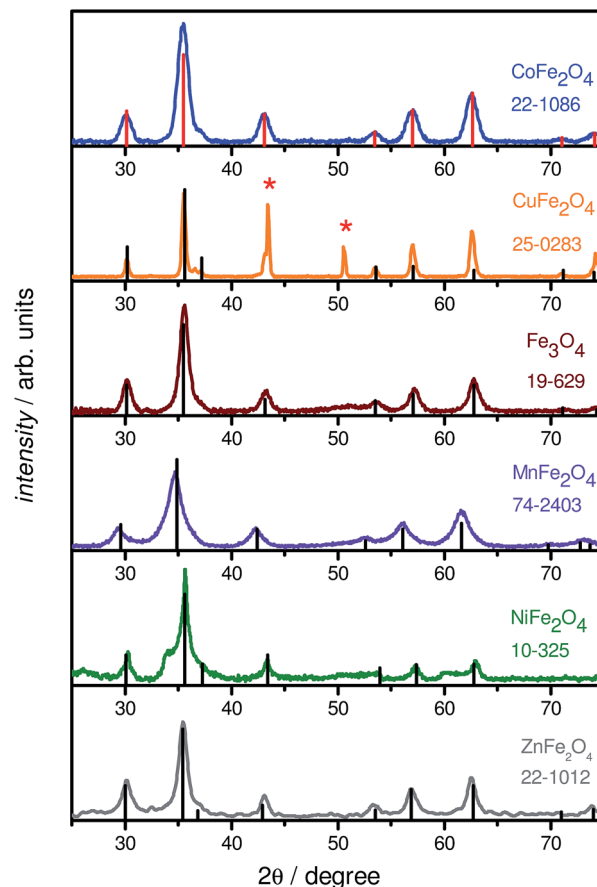
Fig. 2   Powder X-ray diffractograms of the six PEGylated metal ferrites, with superimposed powder patterns obtained from standard JCPDS data for each system. For $CuFe_2O_4$, the peaks attributed to metallic Cu are marked with asterisks.

MFe_2O_4 nanoparticles, along with the corresponding standard line patterns for each ferrite. The XRD analysis revealed that all the samples are spinel cubic in structure (space group: $Fd\bar{3}m$), exhibiting six prominent peaks. A slight shift in peak positions for the substituted spinel NPs with respect to unsubstituted Fe_3O_4 NPs could be noted; this change is well-recorded in literature, and is in agreement with the ionic radii of the divalent cations, indicating a successful incorporation of divalent cations into the lattice.[45] In general, the powder X-ray diffractograms of all the MFe_2O_4 NPs are in excellent agreement with their theoretical counterparts, as can be seen from Fig. 2, the exception being $CuFe_2O_4$, which also showed the presence of Cu^0 NPs. EDXS analysis also confirmed the formation of stoichiometric MFe_2O_4 phases, with the M : Fe ratio being approximately equal to 1 : 2 for all the five ferrite NPs; the $CuFe_2O_4$ NP system, once again, was the slight outlier. As Cu NPs are not expected to be magnetic or only negligibly so,[46] the presence of Cu NPs does not greatly impact the following discussion, with the caveat that all values must be taken as lower limits for $CuFe_2O_4$.

The PEGylated MFe_2O_4 NPs were examined by TEM to assess size and morphology (Fig. 3 and S1†). As can be seen, all the samples contain small spherical NPs (<20 nm in diameter) with
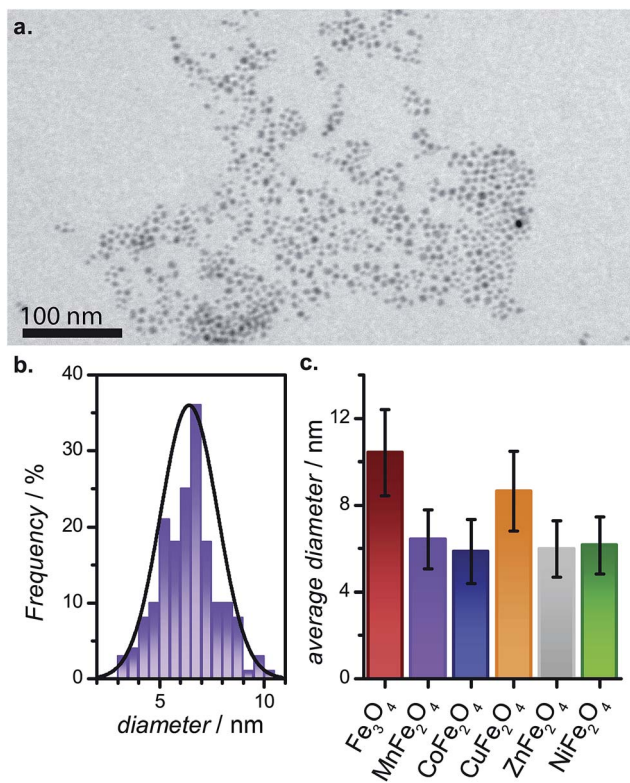
Fig. 1   Synthetic scheme for the one-pot synthesis of super-paramagnetic, PEG$_{400}$-coated MFe_2O_4 (M = Mn, Fe, Co, Ni, Cu, Zn) NPs with sizes ranging from *ca.* 6 to 10 nm.

Fig. 3   (a) Transmission electron micrograph of PEGylated $MnFe_2O_4$ NPs; (b) size distribution for PEGylated $MnFe_2O_4$ NPs generated from the micrographs; and (c) a comparison of the average particle size and standard deviation for the six MFe_2O_4–PEG_{400} NPs studied.

comparable size distributions. The reasonable size mono-dispersity is believed to be controlled by the nucleation and growth of the NP seeds generated upon the rapid addition of $NaBH_4$ to the precursor in PEG medium at high temperatures.

Fig. 4 shows a representative FT-IR spectrum of PEGylated $MnFe_2O_4$ NPs superimposed on the spectrum of neat PEG. It is seen that there are several bands that appear in both the spectra, some of which have been highlighted in the figure: (i)
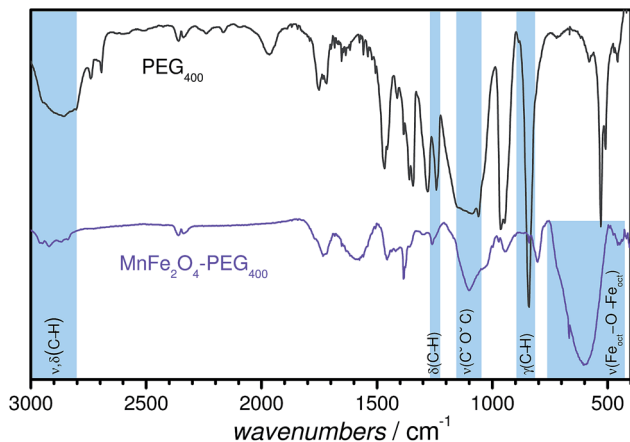
the characteristic absorption band at 950 cm^{-1}, associated with the –CH out-of-plane bending vibrations of PEG; (ii) the absorption band at 1240 cm^{-1}, assigned to C–H twisting in PEG; (iii) the C–O–C ether stretching absorption band at 1094 cm^{-1}; (iv) the bands at ∼2800–3000 cm^{-1}, corresponding to –C–H symmetric and asymmetric stretching vibrations; (v) the band around 2910 cm^{-1}, corresponding to –CH$_2$ stretching vibrations. The C–O–C, –CH$_2$ and –CH peaks confirm the tethering of PEG onto the MFe_2O_4 NP surfaces.[47] The FT-IR spectra of the other PEGylated MFe_2O_4 NPs are shown in Fig. S2.†

3.3   Magnetic characterization

The magnetic properties of the samples were investigated by SQUID magnetometry. For all the magnetic measurements presented here, samples were powdered, and thus the measured magnetic properties represent the average values for an ensemble of randomly oriented nanoparticles. Magnetization *vs.* magnetic field strength loops were recorded at 310, 300 and 1.9 K (310 K: Fig. 5; 300 and 1.9 K: Fig. S3†) for all the metal ferrite samples. In the $M(H)$ curves, hysteresis is observed at 1.9 K, which is characteristic of ferromagnetic behavior, while anhysteretic loops are seen at the physiological temperature, 310 K. The magnetization of the samples was also examined under FC and ZFC conditions. Combined FC–ZFC plots for PEGylated MFe_2O_4 NPs are found in Fig. S4.† All NPs showed blocking temperatures (T_B, indicating the transition from low-temperature, ferromagnetic NPs to freely fluctuating super-paramagnetic NPs at higher temperatures) below room temperature. For all samples, the behavior is typical of super-paramagnetism, which is expected for nanoscaled magnetic NPs.[45] The exception is $CoFe_2O_4$, whose T_B is slightly below room temperature. Upon closer inspection, the room-

Fig. 4   Fourier transform infrared spectra for PEG_{400} and $MnFe_2O_4$–PEG_{400} NPs.
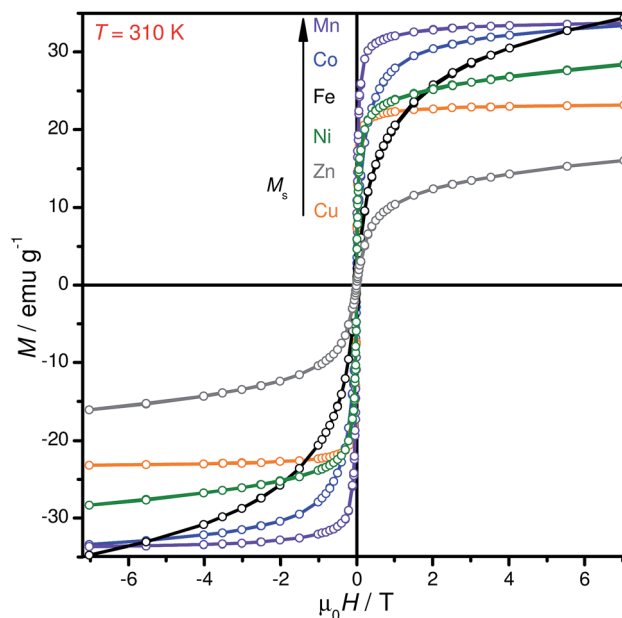

Fig. 5   Measured magnetization *versus* field strength curves for all PEGylated $MnFe_2O_4$ NP samples at 310 K.

Table 1 Summary of magnetometric measurements on PEGylated MFe_2O_4 NPs

Sample	M_s, 310 K (emu g^{-1})	T_B (K)
$MnFe_2O_4$	33.7	47
Fe_3O_4	34.4	150
$CoFe_2O_4$	33.3	280
$NiFe_2O_4$	28.4	150
$CuFe_2O_4$	23.2	61
$ZnFe_2O_4$	16.0	32

temperature $M(H)$ loop for $CoFe_2O_4$ shows a very weak hysteresis. This is consistent with a sample with the majority of NPs in the superparamagnetic state, with a minor component of blocked NPs. The magnetic properties are compiled in Tables 1 and S2.†

In general, the M_s values of our PEGylated MFe_2O_4 NPs were lower than their bulk counterparts: for example, at 300 K, $MnFe_2O_4$–PEG_{400} NPs showed a saturated magnetization M_s of 35.9 emu g^{-1}, which is considerably smaller than the theoretical value of bulk $MnFe_2O_4$ material (110 emu g^{-1}),[48] but very close to the M_s shown by tetraethylene glycol coated 7 nm $MnFe_2O_4$ NPs synthesized by Yang *et al.* The reduced saturation magnetization of NPs is attributed to the existence of a magnetically 'dead' surface layer for each particle in which magnetic moments do not contribute to the magnetization.[49] Given that our $CuFe_2O_4$ NPs had a non-negligible amount of copper contaminant, it is difficult to compare its magnetic properties with the other uncontaminated PEGylated MFe_2O_4 NPs, especially since elemental copper is orders of magnitude less magnetic than $CuFe_2O_4$.[46] A brief discussion on the observed magnetic properties of individual NPs *vis-a-vis* literature is found in the ESI.†

From the M *vs.* H curve of $CoFe_2O_4$ NPs at 1.9 K, it can be clearly seen that they exhibit an anomalous hysteresis behaviour. These broadened hysteresis loops are often seen in nanocomposite systems with strongly coupled soft and hard

magnets; most notably in $CoFe_2O_4$ thin films.[50,51] Ros and co-workers noted a similar broadened hysteresis loop for their ~7 nm $CoFe_2O_4$ NPs, which they attributed to the presence of a strain inhomogeneity from the surface to the core of the NP, leading to the coexistence of soft and hard magnetic behavior within a single particle.[43] The T_B for these NPs, at ~280 K, is also significantly greater than that of the other ferrite NPs; this is expected for $CoFe_2O_4$ NPs.[45,52] The Co^{2+} ion – with a d^7 configuration – imparts a high magnetocrystalline anisotropy from
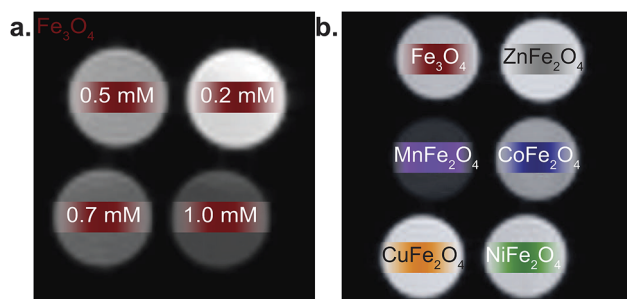

Fig. 7 (a) T_2-weighted image of Fe_3O_4 samples in water at various [Fe] concentrations (b) T_2-weighted image of MFe_2O_4 samples in water.
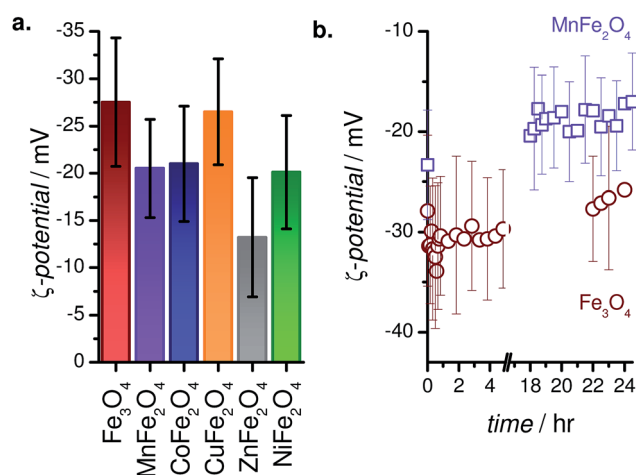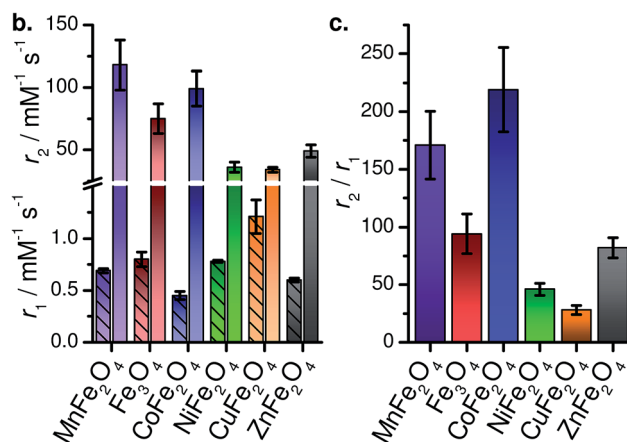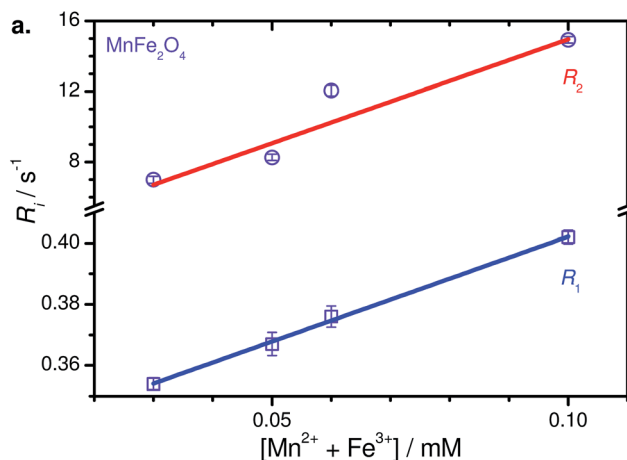

Fig. 8 (a) Relaxometric plot for $MnFe_2O_4$–PEG_{400} NPs in water. (b) Compiled relaxivities (r_1 below the break with hatched bars, r_2 above the break). (c) Compiled r_2/r_1 ratios.

Fig. 6 (a) ζ-Potentials of MFe_2O_4–PEG_{400} NPs in water (pH 7). (b) Temporal evolution of the ζ-potential of Fe_3O_4–PEG_{400} and $MnFe_2O_4$–PEG_{400} NPs in water.

the presence of spin–orbit coupling. The M_s values recorded were 52.8 emu g^{-1} at 1.9 K and 33.7 emu g^{-1} at 300 K.

3.4 Zeta potentials

In order to better understand the physiological stability of MFe$_2$O$_4$–PEG$_{400}$ NPs, zeta potentials (ζ) were measured post-sonication in distilled water at pH $\sim$ 7. The recorded values are compiled in Fig. 6a, and are in accordance with literature precedents, such as the work of Feng et al., who found ζ = −21 mV for their (methoxy polyethylene glycol)-coated Fe$_3$O$_4$ NPs.[53] It is expected that ζ values for these systems might become even higher in physiological buffer owing to protein corona formation and the associated electrosteric repulsion.[54,55] A time-dependent study of the evolution of ζ values for PEGylated Fe$_3$O$_4$ and MnFe$_2$O$_4$ NPs (Fig. 6b) didn't show any drastic changes in the ζ-potential values of these systems over a period of 24 h or more.

3.5 Magnetic resonance imaging

The dispersed solutions of MFe$_2$O$_4$–PEG$_{400}$ NPs in water were used in a relaxometric study to determine the T_1 and T_2 relaxation times, and evaluate their potential as MRI contrast agents. Representative images are show in Fig. 7. As can be seen, contrast increases with concentration (Fig. 7a), while the various MFe$_2$O$_4$ species showed distinct contrast. A sample relaxometric plot for PEGylated MnFe$_2$O$_4$ NPs is shown in Fig. 8, with the relaxation rates R_1 ($=T_1^{-1}$) and R_2 ($=T_2^{-1}$) plotted as a function of the concentration of the magnetic ions in solution. These same measurements for the other samples are shown in Fig. S5.† The effectiveness of NPs as contrast agent is measured in the form of relaxivity, which represents the reciprocal of the relaxation time per unit concentration of magnetic ions (cf. eqn (2)).

This is one of the few systematic investigations of the high-field MRI capabilities in a series of MFe$_2$O$_4$, spanning over six compositions. Of the six MFe$_2$O$_4$–PEG$_{400}$ NPs, MnFe$_2$O$_4$–PEG$_{400}$ NPs are found to be the most effective T_2 contrast agents in aqueous media, with r_1 = 0.69 ± 0.02 mM^{-1} s^{-1}, r_2 = 118 ± 20 mM^{-1} s^{-1}, and r_2/r_1 = 173. Table 2 lists the r_1, r_2, and r_2/r_1 values of the other PEGylated MFe$_2$O$_4$ NPs. CuFe$_2$O$_4$ NPs, laced with elemental copper NPs, show modest contrast-enhancing capabilities which must be considered a lower limit. Interestingly, they show the highest r_1 of the series; as such, further

Table 2 Comparison of NP-based high-field ($B_0 \geq 7$ T) contrast agents

Label[a]	Sample Core	Coating[b]	Size (nm)	B_0 (T)	r_1 (mM^{-1} s^{-1})	r_2 (mM^{-1} s^{-1})	r_2/r_1	Reference
1	Gd$_2$O$_3$	PEG	1.3	11.7	10.4	17.2	1.7	Faucher et al.[57]
2	Gd$_2$O$_3$	DEG	4.6	7	4.4	28.9	6.6	Bridot et al.[58]
3	CoFe$_2$O$_4$@ZnO	Chitosan	11.6	9.4	—	31.8	—	Venkatesha et al.[59]
4	Mn$_{0.29}$Fe$_{2.71}$O$_4$	PEG$_{8000}$	6.5	9	—	32.7	—	Vamvakidis et al.[60]
Cu	CuFe$_2$O$_4$	PEG	8.6	9.4	1.21(16)	34(2)	28(4)	This work
Ni	NiFe$_2$O$_4$	PEG	6.1	9.4	0.78(1)	36(4)	46(5)	This work
Zn	ZnFe$_2$O$_4$	PEG	5.9	9.4	0.60(2)	49(5)	82(9)	This work
5	ZnFe$_2$O$_4$	Chitosan–liposome	≤200	9.4	—	54	—	Hoque et al.[61]
6	Fe$_3$O$_4$	HDA-G2	10	7	—	60	—	Zhao et al.[23]
7	CoFe$_2$O$_4$	Chitosan	8.3	9.4	—	60.9	—	Venkatesha et al.[59]
8	Mn$_{0.35}$Fe$_{2.65}$O$_4$	(1 : 1) 1,2 PG + TEG	6.0	9	—	64.5	—	Vamvakidis et al.[60]
9	ZnFe$_2$O$_4$	PEG	5	9.4	—	68	—	Hoque et al.[61]
Fe	Fe$_3$O$_4$	PEG	10.4	9.4	0.80(7)	75(12)	94(17)	This work
10	ZnFe$_2$O$_4$	Chitosan	4.8	9.4	—	76	—	Hoque et al.[61]
11	NiFe$_2$O$_4$	Chitosan	3	9.4	0.348	89	256	Hoque et al.[62]
Co	CoFe$_2$O$_4$	PEG	5.8	9.4	0.45(4)	99(14)	219(37)	This work
12	NaDyF$_4$	PMAO–PEG	20.3	9.4	0.33	101	306	Das et al.[18]
Mn	MnFe$_2$O$_4$	PEG	6.4	9.4	0.69(2)	118(20)	171(30)	This work
13	Fe$_3$O$_4$	HDA-G2	16	7	—	126	—	Zhao et al.[23]
14	NaHoF$_4$	PMAO–PEG	17	9.4	0.17	130.6	781	Zhang et al.[19]
15	Dy$_2$O$_3$	Dextran	70	7	—	190	—	Norek et al.[63]
16	Fe$_3$O$_4$	Maltol	10.1	9.4	2.11	191	90.5	Clements et al.[30]
17	NiFe$_2$O$_4$	DMSA	9.0	11.7	—	200	—	Menelaou et al.[64]
18	NaDyF$_4$	PMAO–PEG	25 × 35	9.4	0.50	204.4	410	Zhang et al.[19]
19	Fe$_3$O$_4$ octapods	HDA-G2	20	7	—	209	—	Zhao et al.[23]
20	MnFe$_2$O$_4$	Succimer	7.6	9.4	18.6	227.6	12.2	Kim et al.[36]
21	Fe$_3$O$_4$	Succimer	6.0	9.4	11.1	255.9	23.1	Kim et al.[36]
22	NiFe$_2$O$_4$	CTAB	9.0	11.7	—	278.9	—	Menelaou et al.[64]
23	CoFe$_2$O$_4$	Succimer	8.0	9.4	6.3	392.5	62.3	Kim et al.[36]
24	Fe$_3$O$_4$ brick-like	Triton X	64.0	7	4.3	599	139	Worden et al.[24]
—	GdF$_3$	PAA	30–50	9.4	1.44	—	—	Ju et al.[65]

[a] Refers to Fig. 9. [b] DEG: diethylene glycol; PAA: poly(acrylic acid); CTAB: cetyltrimethylammonium bromide; PMAO: poly(maleic anhydride-alt-1-octadecene); HDA-G2: conjugates of dendritic molecules and 1-hexadecylamine; 1,2-PG: 1,2-propylene glycol; TEG: tetraethylene glycol.
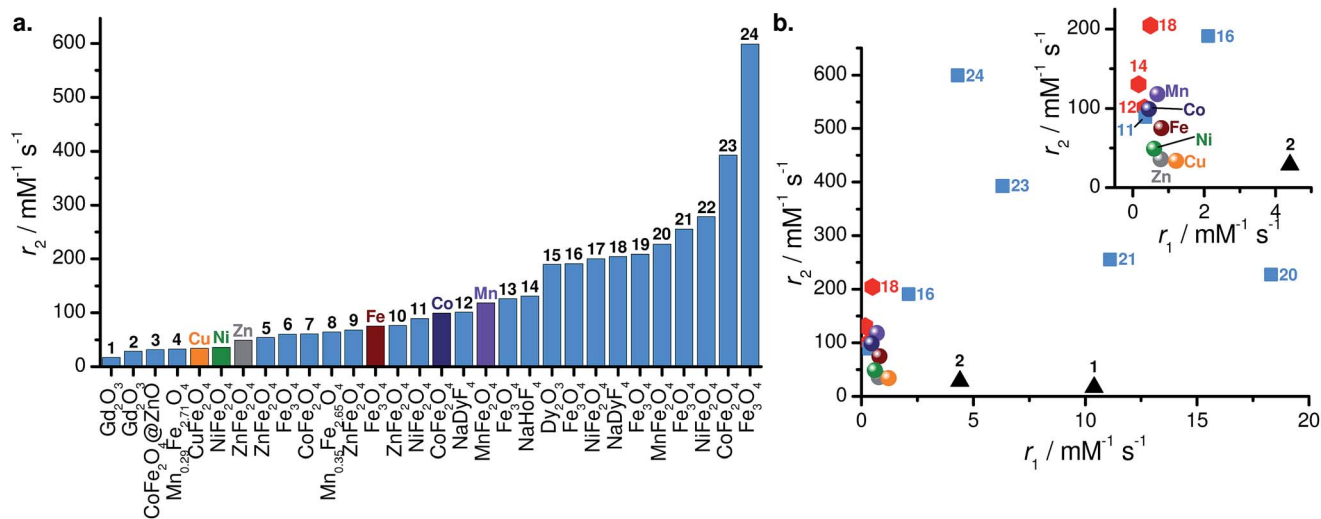
Fig. 9 (a) Comparison of r_2 values and (b) scatter plot of r_1 vs. r_2 for various high-field NP contrast agents. Labels refer to Table 2. In panel (b), spheres: data presented in this work; black triangles: Gd_2O_3 NPs; red hexagons: $NaLnF_4$ NPs; and blue squares: spinel ferrite MFe_2O_4 NPs.

investigation of this species for T_1-weighted MRI may be warranted. We note that to the best of our knowledge, this is only report of $CuFe_2O_4$ NPs used for high-field MRI.

It is evident that $MnFe_2O_4$, $CoFe_2O_4$, and Fe_3O_4 NPs are better T_2 contrast agents compared to $NiFe_2O_4$, $CuFe_2O_4$, and $ZnFe_2O_4$. We generally find that r_2 increases with increased saturation magnetization (Fig. S6†), while the r_1 values are tightly clustered, with no clear trend with respect to magnetization. As may then be expected, the r_2/r_1 ratios track the trend seen for r_2.

While the r_1 and r_2 values of our MFe_2O_4–PEG$_{400}$ NPs are within range with examples in literature (Fig. 9), we believe further improvements are possible by, e.g., templating directional growth to form morphological variations like octapods,[23] bricks,[24] or whiskers;[25] or subjecting them to controlled aggregation and/or self-assembly, which are known to lead to higher contrasting abilities.[56]

Most contrast agents were investigated with clinical MRI scanners (1.5–3 T). Well-know examples include the commercially available Ferridex® and Combidex®. Ferridex® has $r_2 =$ 120 mM^{-1} s^{-1} at a magnetic field of 1.5 T, while the r_2/r_1 increases from 10.1 to 22 when increasing the magnetic field from 1.5 to 3.0 T.[30] Similarly, Combidex® has $r_2 = 65$ mM^{-1} s^{-1} at a magnetic field of 1.5 T, with $r_2/r_1 = 6$.[30]

There are few reports of transition metal ferrite NP contrast agents under high-field conditions; this makes a direct one-to-one comparison with our MFe_2O_4–PEG$_{400}$ NPs at 9.4 T difficult. This difficulty is exacerbated by significant dependencies of magnetic relaxivities on the magnetic field strength,[66] the nature of the solvent (i.e., water vs. plasma vs. buffer), the surface coating,[30,39] aggregation,[56] and magnetic dynamics.[67]

A non-exhaustive compilation of relaxivities of various NP contrast agents used at high fields ($B_0 > 7$ T) is presented in Table 2 and Fig. 9. The nanoparticles in this table can be roughly classified as lanthanide oxides[57,58,63] and fluorides,[65] sodium lanthanide fluorides $NaLnF_4$ (Ln = Ho, Dy),[18,19] and

spinel ferrites.[23,24,30,36,59–61] Upon quick inspection of Fig. 9, it is apparent there is no clear segregation of NP type – or even specific composition – with regards to r_2. As an example, our $MnFe_2O_4$ (Mn) and $CoFe_2O_4$ (Co) NPs are fairly similar in both r_1 and r_2 to $NaHoF_4$ (13)[19] and $NaDyF_4$ (11)[18] (see Fig. 9b). The advantage of the $NaLnF_4$ NPs is their paramagnetic nature; unlike superparamagnetic (i.e. electromagnetically coupled spins), they do not saturate in fields up to 9 T and above. However, their magnetization is substantially lower ($M_s \approx 12$ emu g^{-1} at 7 T for 13 (ref. 19)). In this specific comparison, the two effects seem to balance each other. Another striking example is the comparison of Fe_3O_4–PEG$_{400}$ (Fe) with maltol-coated Fe_3O_4 NP (15).[30] Both have comparable sizes (10.4 vs. 10.1 nm), yet 15 has a r_2 two and a half times that of Fe, despite a lower saturation magnetization (26.8 emu g^{-1}). This discrepancy is attributed to the proximity of water molecules to the magnetic core in 15 due to the small capping ligand.

A compilation of r_2/r_1 ratios is found in Fig. S7.† As can be seen, the ratios found here compare favourably with state-of-the-art. $CoFe_2O_4$ and $MnFe_2O_4$ in particular have high values, showing their promise for use as T_2 high-field contrast agents.

4   Conclusion

In this study, PEGylated sub-15 nm MFe_2O_4 (M = Mn, Fe, Co, Ni, Cu, Zn) NPs were synthesized following a novel protocol, with the capping agent (PEG$_{400}$, a liquid polymer) itself serving as the reaction medium. The NPs were found to be small, fairly monodisperse, and superparamagnetic at room temperature. These NPs were systematically evaluated for high field ($B_0 = 9.4$ T) MRI in vitro. Of the six MFe_2O_4–PEG$_{400}$ NP compositions studied, $MnFe_2O_4$, $CoFe_2O_4$, and Fe_3O_4 NPs displayed superior T_2 contrasting abilities in MRI, with reasonably high r_2 values (~118 mM^{-1} s^{-1} for $MnFe_2O_4$, ~98 mM^{-1} s^{-1} for $CoFe_2O_4$, and ~75 mM^{-1} s^{-1} for Fe_3O_4) and r_2/r_1 ratios (~171 for $MnFe_2O_4$, ~219 for $CoFe_2O_4$, and ~94 for Fe_3O_4). Given the

well-documented biocompatibility of PEG, these transition metal ferrite NP systems deserve to be better investigated as potential contrast agents for dark-field MRI.

Author contributions

ST and AB designed the project, AB and EP carried out the synthetic work and physical characterization, BB and BT oversaw MRI measurements, AB, ST and BT contributed to the writing of the manuscript.

Conflict of interest

There are no conflicts of interest to declare.

Acknowledgements

References

1 E. M. Haacke, R. W. Brown, M. R. Thompson and R. Venkatesan, *Magnetic resonance imaging: physical principles and sequence design*, Wiley-Liss, New York, 1999, vol. 82.

2 B. M. Dale, M. A. Brown and R. C. Semelka, *MRI: basic principles and applications*, John Wiley & Sons, 2015.

3 R. H. Hashemi, W. G. Bradley and C. J. Lisanti, *MRI: the basics*, Lippincott Williams & Wilkins, 2012.

4 G. J. Strijkers, M. Mulder, J. Willem, F. van Tilborg, A. Geralda and K. Nicolay, *Anti-Cancer Agents Med. Chem.*, 2007, **7**, 291–305.

5 C. Rydahl, H. S. Thomsen and P. Marckmann, *Invest. Radiol.*, 2008, **43**, 141–144.

6 E.-K. Lim, T. Kim, S. Paik, S. Haam, Y.-M. Huh and K. Lee, *Chem. Rev.*, 2015, **115**, 327–394.

7 H. B. Na, I. C. Song and T. Hyeon, *Adv. Mater.*, 2009, **21**, 2133–2148.

8 L. Babes, B. Denizot, G. Tanguy, J. J. Le Jeune and P. Jallet, *J. Colloid Interface Sci.*, 1999, **212**, 474–482.

9 B. Blasiak, S. Barnes, T. Foniok, D. Rushford, J. Matyas, D. Ponjevic, W. P. Weglarz, R. Tyson, U. Iqbal, A. Abulrob, G. R. Sutherland, A. Obenaus and B. Tomanek, *BMC Med. Imaging*, 2013, **13**, 20–28.

10 F. Hu and Y. S. Zhao, *Nanoscale*, 2012, **4**, 6235–6243.

11 B. Blasiak, J. Landry, R. Tyson, J. Sharp, U. Iqbal, A. Abulrob, D. Rushford, J. Matyas, D. Ponjevic, G. R. Sutherland, S. Wolfsberger and B. Tomanek, *J. Neurosci. Methods*, 2014, **226**, 132–138.

12 D. Niu, X. Luo, Y. Li, X. Liu, X. Wang and J. Shi, *ACS Appl. Mater. Interfaces*, 2013, **5**, 9942–9948.

13 C. Mainero, T. Benner, A. Radding, A. Van Der Kouwe, R. Jensen, B. Rosen and R. Kinkel, *Neurology*, 2009, **73**, 941–948.

14 R. R. Regatte and M. E. Schweitzer, *J. Magn. Reson. Imag.*, 2007, **25**, 262–269.

15 T. Nakada, *Brain Dev.*, 2007, **29**, 325–335.

16 P. Stanwell, L. Gluch, D. Clark, B. Tomanek, L. Baker, B. Giuffrè, C. Lean, P. Malycha and C. Mountford, *Eur. Radiol.*, 2005, **15**, 1037–1043.

17 B. Blasiak, F. C. van Veggel and B. Tomanek, *J. Nanomater.*, 2013, **2013**, 148578.

18 G. K. Das, N. J. Johnson, J. Cramen, B. Blasiak, P. Latta, B. Tomanek and F. Van Veggel, *J. Phys. Chem. Lett.*, 2012, **3**, 524–529.

19 X. Zhang, B. Blasiak, A. J. Marenco, S. Trudel, B. Tomanek and F. C. J. M. van Veggel, *Chem. Mater.*, 2016, **28**, 3060–3072.

20 Y.-w. Jun, Y.-M. Huh, J.-s. Choi, J.-H. Lee, H.-T. Song, K. Kim, S. Yoon, K.-S. Kim, J.-S. Shin, J.-S. Suh and J. Cheon, *J. Am. Chem. Soc.*, 2005, **127**, 5732–5733.

21 S. Balasubramaniam, S. Kayandan, Y.-N. Lin, D. F. Kelly, M. J. House, R. C. Woodward, T. G. S. Pierre, J. S. Riffle and R. M. Davis, *Langmuir*, 2014, **30**, 1580–1587.

22 J. Zeng, L. Jing, Y. Hou, M. Jiao, R. Qiao, Q. Jia, C. Liu, F. Fang, H. Lei and M. Gao, *Adv. Mater.*, 2014, **26**, 2694–2698.

23 Z. Zhao, Z. Zhou, J. Bao, Z. Wang, J. Hu, X. Chi, K. Ni, R. Wang, X. Chen and Z. Chen, *Nat. Commun.*, 2013, **4**, 2266.

24 M. Worden, M. A. Bruckman, M.-H. Kim, N. F. Steinmetz, J. M. Kikkawa, C. LaSpina and T. Hegmann, *J. Mater. Chem. B*, 2015, **3**, 6877–6884.

25 T. Macher, J. Totenhagen, J. Sherwood, Y. Qin, D. Gurler, M. S. Bolding and Y. Bao, *Adv. Funct. Mater.*, 2015, **25**, 490–494.

26 J. Mohapatra, A. Mitra, H. Tyagi, D. Bahadur and M. Aslam, *Nanoscale*, 2015, **7**, 9174–9184.

27 L. A. Thomas, L. Dekker, M. Kallumadil, P. Southern, M. Wilson, S. P. Nair, Q. A. Pankhurst and I. P. Parkin, *J. Mater. Chem.*, 2009, **19**, 6529–6535.

28 C.-L. Liu, Y.-K. Peng, S.-W. Chou, W.-H. Tseng, Y.-J. Tseng, H.-C. Chen, J.-K. Hsiao and P.-T. Chou, *Small*, 2014, **10**, 3962–3969.

29 C. Xu, K. Xu, H. Gu, R. Zheng, H. Liu, X. Zhang, Z. Guo and B. Xu, *J. Am. Chem. Soc.*, 2004, **126**, 9938–9939.

30 T. W. Clements, C. Sarsons, C. M. Platnich, A. Banerjee, B. Blasiak, B. Tomanek, K. D. Rinker and S. Trudel, *ChemistrySelect*, 2016, **1**, 1602–1606.

31 K. V. Korpany, F. Habib, M. Murugesu and A. S. Blum, *Mater. Chem. Phys.*, 2013, **138**, 29–37.

32 K. V. Korpany, C. Mottillo, J. Bachelder, S. N. Cross, P. Dong, S. Trudel, T. Friscic and A. S. Blum, *Chem. Commun.*, 2016, **52**, 3054–3057.

33 M. Zhang, X. Li, Y. Gong, N. Zhao and X. Zhang, *Biomaterials*, 2002, **23**, 2641–2648.

34 N. A. Alcantar, E. S. Aydil and J. N. Israelachvili, *J. Biomed. Mater. Res.*, 2000, **51**, 343–351.

35 J.-H. Lee, Y.-M. Huh, Y.-w. Jun, J.-w. Seo, J.-t. Jang, H.-T. Song, S. Kim, E.-J. Cho, H.-G. Yoon, J.-S. Suh and J. Cheon, *Nat. Med.*, 2007, **13**, 95–99.

36 D.-H. Kim, H. Zeng, T. C. Ng and C. S. Brazel, *J. Magn. Magn. Mater.*, 2009, **321**, 3899–3904.

37 M. Menelaou, Z. Iatridi, I. Tsougos, K. Vasiou, C. Dendrinou-Samara and G. Bokias, *Dalton Trans.*, 2015, **44**, 10980–10990.

38 N. Lee and T. Hyeon, *Chem. Soc. Rev.*, 2012, **41**, 2575–2589.

39 S. Tong, S. Hou, Z. Zheng, J. Zhou and G. Bao, *Nano Lett.*, 2010, **10**, 4607–4613.

40 A. R. West, *Basic Solid State Chemistry*, John Wiley & Sons, 1999.

41 V. Yathindranath, L. Rebbouh, D. F. Moore, D. W. Miller, J. van Lierop and T. Hegmann, *Adv. Funct. Mater.*, 2011, **21**, 1457–1464.

42 M. Abràmoff, P. Magalhães and S. Ram, *Biophoton. Int.*, 2004, **11**, 36–42.

43 E. Solano, L. Perez-Mirabet, F. Martinez-Julian, R. Guzmán, J. Arbiol, T. Puig, X. Obradors, R. Yañez, A. Pomar, S. Ricart and J. Ros, *J. Nanopart. Res.*, 2012, **14**, 1034.

44 E. Solano, R. Yáñez, S. Ricart and J. Ros, *J. Magn. Magn. Mater.*, 2015, **382**, 380–385.

45 A. L. Tiano, G. C. Papaefthymiou, C. S. Lewis, J. Han, C. Zhang, Q. Li, C. Shi, A. M. M. Abeykoon, S. J. L. Billinge, E. Stach, J. Thomas, K. Guerrero, P. Munayco, J. Munayco, R. B. Scorzelli, P. Burnham, A. J. Viescas and S. S. Wong, *Chem. Mater.*, 2015, **27**, 3572–3592.

46 A. J. Marenco, D. B. Pedersen and S. Trudel, *J. Phys. Chem. C*, 2016, **120**, 7388–7396.

47 Y. Zhang, N. Kohler and M. Zhang, *Biomaterials*, 2002, **23**, 1553–1561.

48 D. Carta, M. F. Casula, A. Falqui, D. Loche, G. Mountjoy, C. Sangregorio and A. Corrias, *J. Phys. Chem. C*, 2009, **113**, 8606–8615.

49 M. Unni, A. M. Uhl, S. Savliwala, B. H. Savitzky, R. Dhavalikar, N. Garraud, D. P. Arnold, L. F. Kourkoutis, J. S. Andrew and C. Rinaldi, *ACS Nano*, 2017, **11**, 2284–2303.

50 S. Xie, J. Cheng, B. Wessels and V. Dravid, *Appl. Phys. Lett.*, 2008, **93**, 181901.

51 F. Rigato, J. Geshev, V. Skumryev and J. Fontcuberta, *J. Appl. Phys.*, 2009, **106**, 113924.

52 S. Trudel and R. Hill, *Polyhedron*, 2007, **26**, 1863–1870.

53 X. Cao, B. Zhang, F. Zhao and L. Feng, *J. Nanomater.*, 2012, **2012**, 1.

54 M. Ravichandran, G. Oza, S. Velumani, J. T. Ramirez, F. Garcia-Sierra, N. B. Andrade, M. A. Garza-Navarro, D. I. Garcia-Gutierrez, R. Lara-Estrada and E. Sacristán-Rock, *RSC Adv.*, 2015, **5**, 17223–17227.

55 P. Del Pino, B. Pelaz, Q. Zhang, P. Maffre, G. U. Nienhaus and W. J. Parak, *Mater. Horiz.*, 2014, **1**, 301–313.

56 S. Singamaneni, V. N. Bliznyuk, C. Binek and E. Y. Tsymbal, *J. Mater. Chem.*, 2011, **21**, 16819–16845.

57 L. Faucher, M. Tremblay, J. Lagueux, Y. Gossuin and M. A. Fortin, *ACS Appl. Mater. Interfaces*, 2012, **4**, 4506–4515.

58 J.-L. Bridot, A.-C. Faure, S. Laurent, C. Rivière, C. Billotey, B. Hiba, M. Janier, V. Josserand, J.-L. Coll, L. Vander Elst, R. Muller, S. Roux, P. Perriat and O. Tillement, *J. Am. Chem. Soc.*, 2007, **129**, 5076–5084.

59 N. Venkatesha, Y. Qurishi, H. S. Atreya and C. Srivastava, *RSC Adv.*, 2016, **6**, 18843–18851.

60 K. Vamvakidis, M. Katsikini, G. Vourlias, M. Angelakeris, E. C. Paloura and C. Dendrinou-Samara, *Dalton Trans.*, 2015, **44**, 5396–5406.

61 S. M. Hoque, M. S. Hossain, S. Choudhury, S. Akhter and F. Hyder, *Mater. Lett.*, 2016, **162**, 60–63.

62 S. M. Hoque, M. Tariq, S. I. Liba, F. Salehin, Z. H. Mahmood, M. N. I. Khan, K. Chattopadhayay, R. Islam and S. Akhter, *Nanotechnology*, 2016, **27**, 285702.

63 M. Norek, E. Kampert, U. Zeitler and J. A. Peters, *J. Am. Chem. Soc.*, 2008, **130**, 5335–5340.

64 M. Menelaou, K. Georgoula, K. Simeonidis and C. Dendrinou-Samara, *Dalton Trans.*, 2014, **43**, 3626–3636.

65 Q. Ju, Y. S. Liu, D. T. Tu, H. M. Zhu, R. F. Li and X. Y. Chen, *Chem.–Eur. J.*, 2011, **17**, 8549–8554.

66 M. Rohrer, H. Bauer, J. Mintorovitch, M. Requardt and H.-J. Weinmann, *Invest. Radiol.*, 2005, **40**, 715–724.

67 P. Caravan, C. T. Farrar, L. Frullano and R. Uppal, *Contrast Media Mol. Imaging*, 2009, **4**, 89–100.